Journal of Materials Chemistry A

ROYAL SOCIETY OF CHEMISTRY

PAPER

View Article Online
View Journal | View Issue

Check for updates

Cite this: J. Mater. Chem. A, 2024, 12, 25887

# Boosted $Li_2CO_3$ reversible conversion utilizing Cu-doped TiB MBene/graphene for Li–$CO_2$ batteries†

Tingting Luo,[a] Qiong Peng, *[a] Mengmeng Yang,[a] Haojie Hu,[a] Junfei Ding,[a] Yanli Chen,[a] Xiu Gong,[a] Jingliang Yang,[a] Yunpeng Qu,[a] Zeyou Zhou,[b] Xiaosi Qi *[a] and Zhimei Sun *[c]

Two-dimensional transition metal borides (MBenes), particularly TiB, hold promise as electrocatalysts for $CO_2$-related reactions. However, their bifunctional catalytic performance for reversible $Li_2CO_3$ conversion in Li–$CO_2$ batteries remains inferior to that of Ru-based catalysts. We addressed this issue by introducing tensile strain and doping late transition metal atoms (Mn, Fe, Co, Ni, Cu) into the basal plane of a TiB MBene/graphene heterostructure. Spin-polarized density functional theory (DFT) calculations revealed that the Cu-doped TiB/graphene catalyst (Cu/$Ti_{17}B_{18}$/G) exhibits an ultralow $CO_2$ reduction and evolution overpotential of 0.66 V, enhancing $Li_2CO_3$ nucleation and reversible conversion with carbon products. This improvement is attributed to weakened adsorption of O-containing intermediates on the Cu-doped surface, facilitated by the down-shifted d-band center and increased antibonding state occupancy. Consequently, Cu/$Ti_{17}B_{18}$/G emerges as a promising bifunctional electrocatalyst for Li–$CO_2$ batteries, outperforming pristine TiB/G and other reported catalysts. Furthermore, its bifunctional activity can be further improved by applying *x*-direction tensile strain. Molecular dynamics simulations combined with explicit solvent models further confirmed the catalytic durability and stability of Cu/$Ti_{17}B_{18}$/G in solution. This work provides valuable atomic-scale insights for exploring advanced Li–$CO_2$ battery catalysts.

Received 31st July 2024
Accepted 2nd September 2024

DOI: 10.1039/d4ta05343e

rsc.li/materials-a

Published on 02 Waysu 2024. Downloaded on 28/07/2025 6:18:09 AM.

## 1. Introduction

The aprotic Li–$CO_2$ battery, owing to its high theoretical energy density of up to 1876 mA h $g^{-1}$ and its $CO_2$ neutralization capability, is one of the most promising energy storage and conversion technologies.[1–3] The discharge/charge process involves a reversible $Li_2CO_3$ nucleation/decomposition reaction (*i.e.*, $CO_2$ reduction/evolution reaction, $CO_2$RR/$CO_2$ER), represented by the reaction: $4Li + 3CO_2 \rightleftarrows 2Li_2CO_3 + C$.[4–6] However, the sluggish kinetics and incomplete reactions lead to the accumulation of $Li_2CO_3$ products and the generation of reactive oxygen species, which can block active sites and diminish battery efficiency.[7–10] Additionally, the inert nature of $CO_2$ and the wide bandgap of $Li_2CO_3$ present pronounced activation energy barriers, directly limiting the reversible $Li_2CO_3$ conversion in Li–$CO_2$ batteries.[11,12] Therefore, it is desirable yet challenging to develop highly active and stable bifunctional electrocatalysts that not only drive the $CO_2$ activation but also facilitate the $Li_2CO_3$ nucleation and reversible decomposition with carbon products.[13–15]

Two-dimensional (2D) orthorhombic transition metal borides (MBenes) have been widely explored as potential catalysts in diverse electrochemical reactions ascribed to their outstanding electrical conductivity and abundance of active sites.[16–19] Among these, titanium boride (TiB) stands out as it has been successfully synthesized and is the lightest MBene, making it highly suitable for portable and lightweight battery applications.[16,20] Notably, Mir *et al.* demonstrated that TiB exhibits stronger adsorption energies compared to VB, CrB, MnB, and FeB, along with excellent electrical conductivity and dynamic stability, making it highly effective for $CO_2$ capture and activation.[20,21] Our recent research further revealed the inherent catalytic activity of 2D TiB basal plane for converting $CO_2$ into $Li_2CO_3$ and carbon products.[22] This activity is facilitated by the bidirectional electron transfer between $CO_2$ reactants and the TiB surface. Unfortunately, the bifunctional catalytic performance of TiB still lags behind that of noble metal Ru-based catalysts. A significant limitation is the excessive adsorption of Li/C/O intermediates on the TiB plane, which hampers the reversible conversion of $Li_2CO_3$.

In this study, we aim to overcome these limitations by doping late transition metals (TM = Mn, Fe, Co, Ni, Cu) into the basal plane of TiB MBene and coupling this modified structure with graphene to form a stable heterostructure. The use of late

[a]College of Physics, Guizhou University, Guiyang 550025, China. E-mail: qpeng@gzu.edu.cn; xsqi@gzu.edu.cn

[b]State Grid Fujian Electric Power Research Institute, Fuzhou 350007, China

[c]School of Materials Science and Engineering, Beihang University, Beijing 100191, China. E-mail: zmsun@buaa.edu.cn

† Electronic supplementary information (ESI) available. See DOI: https://doi.org/10.1039/d4ta05343e

Published on 02 Waysu 2024. Downloaded on 28/07/2025 6:18:09 AM.

transition metals with paired d electrons can facilitate electron compensation with the empty or unpaired d orbitals of Ti atoms in the TiB plane, which is expected to balance the adsorption strength of intermediates on the catalytic surface.[22] In addition, among the catalysts studied so far, Cu remains the only heterogeneous electrocatalyst for selective $CO_2$ electroreduction to multicarbon ($C_{2+}$) products.[23,24] Therefore, doping with late transition metals, particularly Cu, which has fully paired d-electrons, is anticipated to reshape the electronic structure of TiB and alleviate the excessive adsorption of Li/C/O intermediates on the TiB plane. Using spin-polarized density functional theory (DFT) calculations, we first investigate the stability of late transition metals-doped TiB/graphene heterostructures (TM/$Ti_{17}B_{18}$/G, TM = Mn, Fe, Co, Ni, Cu). Subsequently, we explore the electrochemical reaction mechanisms in Li–$CO_2$ batteries. Notably, the Cu/$Ti_{17}B_{18}$/G catalyst delivers optimal bifunctional catalytic activity for $Li_2CO_3$ nucleation and reversible conversion, achieving an ultralow overpotential of 0.66 V. Furthermore, tensile strain is applied to tailor the d-band center and enhance the bifunctional activity of the catalyst. Finally, molecular dynamics simulations are conducted to assess the catalytic durability of the Cu/$Ti_{17}B_{18}$/G heterostructure in solution. This research provides valuable insights into the atomic-level interactions and mechanisms that drive the improved $Li_2CO_3$ reversible conversion performance of Cu-doped TiB MBene/graphene electrocatalysts, paving the way for the development of advanced multifunctional catalysts for next-generation Li–$CO_2$ batteries.

## 2. Computational methods and models

Utilizing the Vienna *Ab initio* Simulation Package (VASP),[25–27] spin-polarized density functional theory (DFT) calculations were conducted to investigate the structural stability and electrocatalytic properties. The ALKEMIE[28] and VASPKIT[29] codes were implemented to postprocess the computational data. The PBE-D3 exchange–correlation[30] was chosen to elucidate the interaction dynamics between reaction intermediates and catalytic active sites.[31] The plane wave cut-off energy was set at 500 eV. All configurations were based on a 4 × 4 supercell of graphene and 3 × 3 supercell of TiB with a vacuum slab of 25 Å inserted in the $z$ direction to prevent interaction between two neighboring surfaces. Crystal orbital Hamilton population (COHP) analyses were performed using the LOBSTER package.[32] Furthermore, the Bader charge analysis was applied to quantify the charge transfer.[33,34] To capture each saddle-point structure and the associated minimum energy path during the oxidative dissociation of $Li_2CO_3$, climbing image nudged elastic band (CINEB) calculations were performed.[35] *Ab initio* molecular dynamics (AIMD) simulations were conducted to assess the thermodynamic stability under reaction conditions at 300 K for a duration of 10 ps, with a time step of 2 fs.[36] In this simulation, tetraethylene glycol dimethyl ether (TEGDME, $CH_3O(CH_2CH_2O)_4CH_3$), with a density of 1.007 g $cm^{-3}$ and low dielectric permittivity of 7.79,[37] was utilized as the organic solvation medium.[38] The radial distribution function $g(r)$ and the coordination number[39] were obtained using the VASPKIT code.

The TiB/G heterostructure consists of 18 Ti atoms, 18 B atoms, and 32 C atoms; the lattice parameters of TiB and graphene are outlined in Table S1 of (ESI).† Subsequently, a single Ti atom was removed from TiB/G to anchor a late transition metal (TM) atom, such as Mn, Fe, Co, Ni and Cu. The thermodynamic stability of TM/$Ti_{17}B_{18}$/G systems was confirmed by the negative formation energy ($E_f$) (Table S2†), which was calculated using the following equation:

$$E_f = E_{TM/Ti_{17}B_{18}/G} - E_{Ti_{17}B_{18}/G} - E_{TM}^{bulk} \quad (1)$$

where $E_{TM/Ti_{17}B_{18}/G}$ and $E_{Ti_{17}B_{18}/G}$ denote the energies of TM/$Ti_{17}B_{18}$/G composite and $Ti_{17}B_{18}$/G substrate, respectively, and $E_{TM}^{bulk}$ represents the total energy of the bulk metal. Additionally, the electrochemical stability of the TM/$Ti_{17}B_{18}$/G catalysts was evaluated using the following formula:

$$U_{diss} = U_{diss}^0 - E_b/N_e \quad (2)$$

where $U_{diss}^0$ and $N_e$ refer to the standard electrode potential of bulk metal and the number of electrons transferred in the dissolution process, respectively. As shown in Table S3,† the $U_{diss}$ is greater than 0 V (*vs.* SHE), indicating that the considered TM/$Ti_{17}B_{18}$/G catalysts are electrochemically stable. The $E_b$ represents the binding energy obtained from the following equation:

$$E_b = E_{TM/Ti_{17}B_{18}/G} - E_{Ti_{17}B_{18}/G} - E_{TM}^{isolated} \quad (3)$$

where $E_{TM}^{isolated}$ is the energy of an isolated transition metal. A more negative $E_b$ value denotes stronger adsorption of the metal atom on the defective TiB/G substrate. In addition, the stress–strain and energy–strain methodologies were employed to investigate the mechanical properties.[40–43] When a uniaxial stress was imposed in the $x$ or $y$ directions, the strain was defined as:

$$\varepsilon = \frac{a - a_0}{a_0} \times 100\% \quad (4)$$

here, $a$ and $a_0$ signify the lattice constants of the strained and unstrained systems.

To monitor the reaction process on different catalysts, the Gibbs free energies of Li–$CO_2$ reaction intermediates were calculated using eqn (5).[44] Particularly, in the Li–$CO_2$ batteries, $Li^+ + e^- \rightleftarrows Li$ is in equilibrium with bulk Li at 0 V.

$$\Delta G = \Delta E_{DFT} + \Delta E_{ZPE} - T\Delta S + neU \quad (5)$$

where $\Delta E_{DFT}$, $\Delta E_{ZPE}$ and $\Delta S$ are the DFT total energy difference, zero-point energy change, and entropy change at $T = 298.15$ K, respectively, which are given in Tables S4–S6.† The term $U$ stands for the applied electrode potential, and $n$ represents the number of transferred electrons. For the Li–$CO_2$ battery, the discharge potential ($U_{DC}$) during $CO_2$RR and charge potential ($U_C$) during $CO_2$ER correspond to the minimum/maximum potentials required to sustain the redox processes. The

 This journal is © The Royal Society of Chemistry 2024

Published on 02 Waysu 2024. Downloaded on 28/07/2025 6:18:09 AM.

deviation between the discharge/charge potential and theoretical equilibrium potential ($U_{eq}$ = 2.87 V) signifies the $CO_2$RR/$CO_2$ER overpotentials, *i.e.*, $\eta_{CO_2RR} = U_{eq} - U_{DC}$ and $\eta_{CO_2ER} = U_C - U_{eq}$. Herein, we applied the total overpotentials for $CO_2$RR and $CO_2$ER ($\eta_{tot} = \eta_{CO_2RR} + \eta_{CO_2ER}$) as a quantitative metric to assess the bifunctional activity of targeted catalysts for Li–$CO_2$ redox.

# 3. Results and discussion

## 3.1. Insight into TiB MBene material design

Fig. 1a presents the material design idea of late transition metal Cu doped TiB MBene/graphene heterostructure to alleviate the adsorption strength of Li/C/O intermediates. Taking advantage of the unique electronic configuration of late transition metals, Cu dopant is expected to serve as a d-electron buffer. Moreover, the maximum lattice mismatch between TiB with 3 × 3 supercell and graphene with $2\sqrt{3} \times 4$ supercell was found to be 4.18%, demonstrating they are good counterparts for establishing high-quality heterostructures. The negative formation energy in Fig. 1b signifies the thermodynamical stability of transition metals Mn, Fe, Co, Ni, Cu doped TiB/graphene heterostructures (TM/$Ti_{17}B_{18}$/G). As demonstrated by Jang *et al.*,[45] $sp^2$ hybridized graphene can capture electrons from the metal layer, resulting in strong interface coupling that stabilizes the metal catalyst and modifies its electronic properties. Indeed, there are abundant electrons localized at the Cu/$Ti_{17}B_{18}$/G heterointerface, and graphene capture 3.46 electrons from the Cu/$Ti_{17}B_{18}$ layer (Fig. S1†), suggesting a strong coupling between them. The Cu dopant exhibits a lower d-band center ($\varepsilon_d$) of −2.78 eV in comparison with pristine TiB/G ($\varepsilon_d$ = −2.55 eV). According to the d-band center theory,[46–48] the down-shifted $\varepsilon_d$ signifies a weakened binding capability of the active site for reaction intermediates. Therefore, a lower d-band center in Cu/$Ti_{17}B_{18}$/G holds promise for alleviating the intense intermediate adsorption issue on the pristine TiB surface. Next, we will confirm this idea using the spin-polarized DFT calculations and constant potential solvation models in ESI.†

## 3.2. Reaction mechanism and electrocatalytic performance

Promising bifunctional catalysts should strike a balance between the $CO_2$ reduction and evolution, *i.e.*, $Li_2CO_3$ generation and its reversible dissociation. Fig. S2† lists several possible pathways for $CO_2$ reduction to $Li_2C_2O_4$ and $Li_2CO_3$ during the initial $2e^-$ step of the discharging process. Prior studies have shown that the nucleation selectivity of $Li_2CO_3$ and $Li_2C_2O_4$ is dependent on the applied catalysts.[5,49] For each reaction intermediate, distinct adsorption configurations are taken into account in Fig. S3† and the energetically optimal one is displayed in Fig. 2a. Worth noting that the *$Li_2C_2O_4$ nucleation is not as stable as that of *$Li_2CO_3$ on both TiB/G and Cu/$Ti_{17}B_{18}$/G surfaces, which is prone to decompose into *$Li_2CO_3$ and *CO, regardless of the specific $CO_2$ reduction pathway. This disproportionation splitting is energetically favorable, with an exothermic free energy change of −1.25 eV on TiB/G surface and −2.21 eV on Cu/$Ti_{17}B_{18}$/G surface. Thus, *$Li_2CO_3$ is identified as the final discharge product for TiB/G and Cu/$Ti_{17}B_{18}$/G use in Li–$CO_2$ batteries, analogue to Ru(0001) catalyst.[50] Generally, a catalyst with $Li_2CO_3$ nucleation selectivity is promising for achieving efficient four-electron ($4e^-$) $CO_2$ reduction ($4Li^+ + 3CO_2 + 4e^- \rightarrow 2Li_2CO_3 + C$) in Li–$CO_2$ batteries.[51,52]

For the reverse $CO_2$ evolution process, the dissociation of $Li_2CO_3$ and the participation of amorphous carbon products play

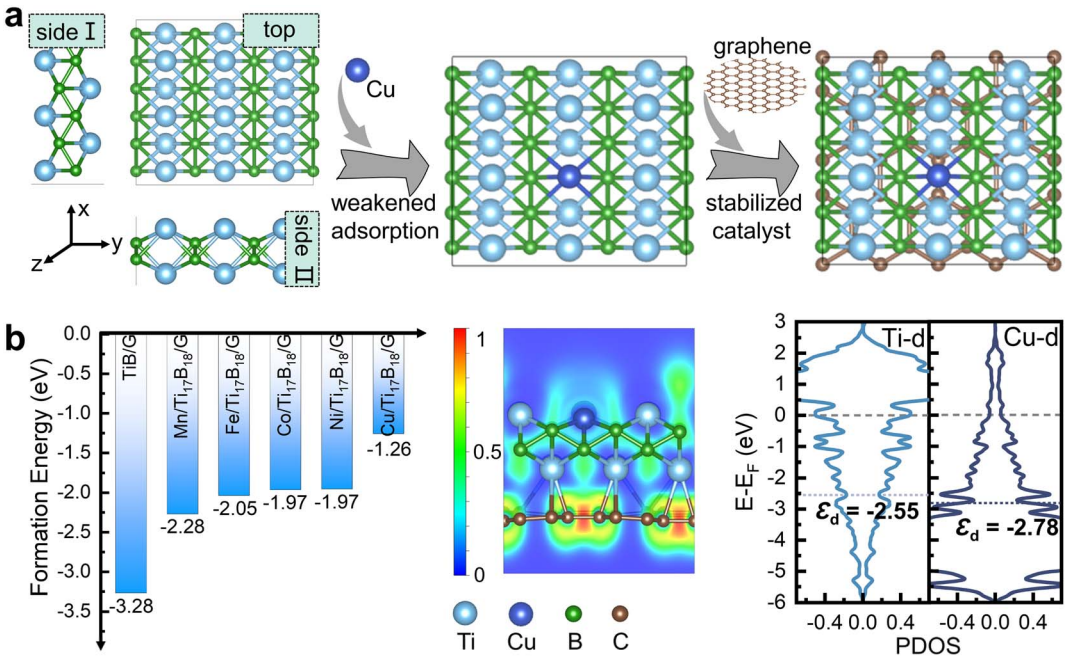


Fig. 1 (a) Schematic of the TiB MBene/graphene heterostructure design. (b) Formation energy of late transition metal atoms (Mn, Fe, Co, Ni, Cu) doped TiB/G heterostructure and electronic properties of Cu/$Ti_{17}B_{18}$/G.

Published on 02 Waysu 2024. Downloaded on 28/07/2025 6:18:09 AM.

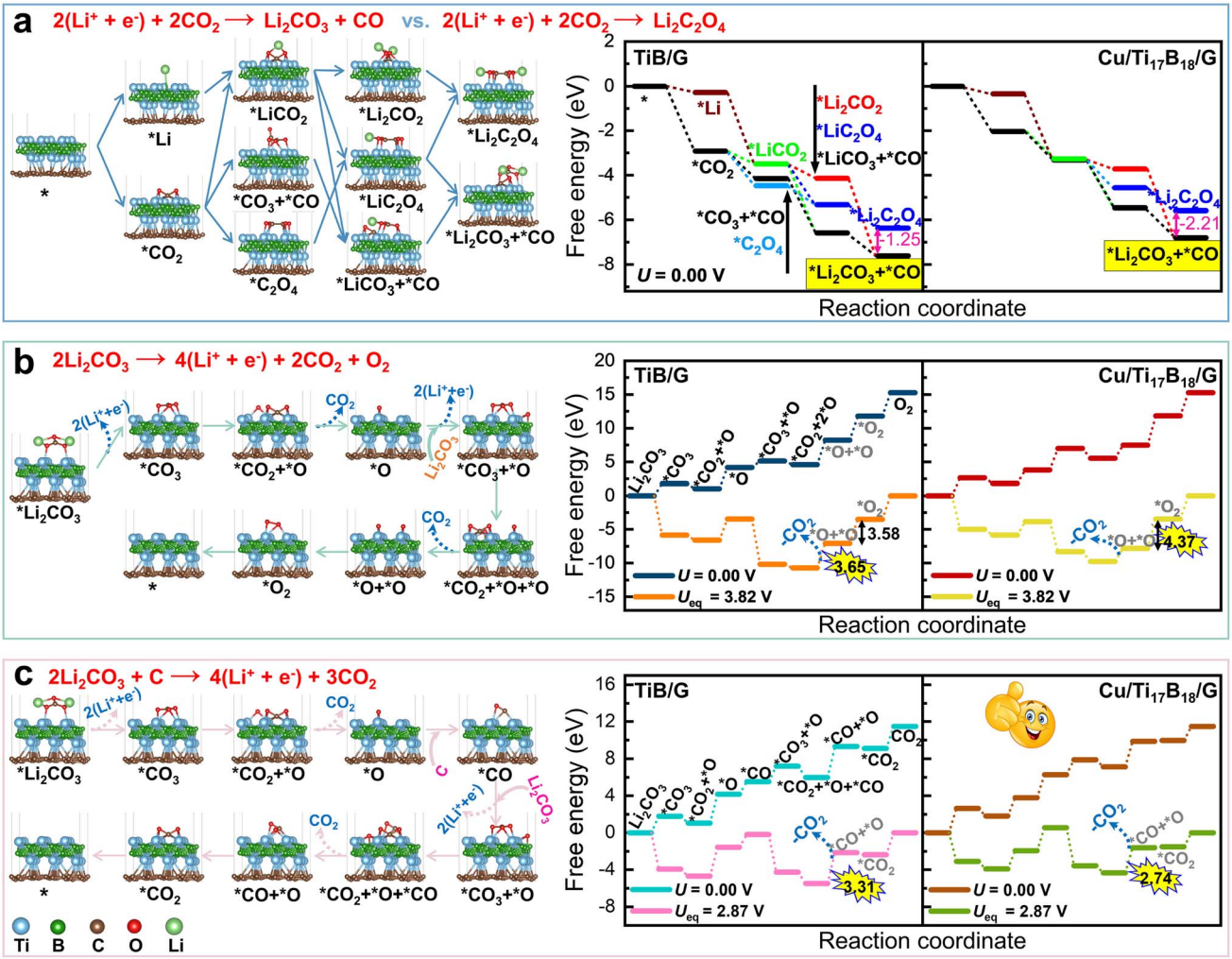


Fig. 2 (a) Nucleation selectivity of $*Li_2C_2O_4$ and $*Li_2CO_3$ on pristine and Cu-doped TiB/G catalysts. (b) Self-decomposition of $Li_2CO_3$ to evolve $O_2$. (c) The co-decomposition of $Li_2CO_3$ and carbon to regenerate original reactants, where the rate-determining step is highlighted.

a decisive role in the cycling stability of Li–$CO_2$ batteries.[53] If amorphous carbon is not involved in the $Li_2CO_3$ decomposition, aggressive oxygen species will be generated and accumulated, passivating the electrocatalysts.[54] As depicted in Fig. S4,† Cu/$Ti_{17}B_{18}$/G exhibits a much lower energy barrier (1.09 eV) for $Li_2CO_3$ decomposition, in comparison with that of graphene-based single-atom catalyst Cr@G (1.67 eV), single-layer $MoS_2$ (2.63 eV), and $ReS_2$ (2.36 eV) catalysts.[55,56] The free energy changes associated with the self-decomposition of $Li_2CO_3$ or its co-oxidative dissociation with carbon products are graphically illustrated in Fig. 2b and c. Evidently, when carbon products engage in the $Li_2CO_3$ decomposition through the oxidative reaction $2Li_2CO_3 + C \rightarrow 4Li^+ + 3CO_2 + 4e^-$, the Cu/$Ti_{17}B_{18}$/G catalyst presents the lowest rate-determining step (RDS) energy barrier of 2.74 eV. These findings indicate that the Cu/$Ti_{17}B_{18}$/G catalyst possesses the dual capability of facilitating the selective $Li_2CO_3$ nucleation and efficiently promoting its reversible dissociation to original reactants, meriting further exploration.

Therefore, to assess the bifunctional $CO_2$RR/$CO_2$ER activity of TiB/G and Cu/$Ti_{17}B_{18}$/G in Li–$CO_2$ batteries, a continuous four-electron transfer mechanism is adopted in Fig. 3a. During the initial $2e^-$ step of the discharge process, $CO_2$ and $Li^+$ are co-adsorbed on the catalyst surface to yield $*LiCO_2$ intermediate, which then reacts with additional $Li^+$ and $CO_2$ to form the first $Li_2CO_3$ product and *CO intermediate. In the subsequent $2e^-$ step, the *CO further reacts with two $Li^+$ and one $CO_2$ molecule to produce the second $Li_2CO_3$ and amorphous C.[13] As seen in Fig. S5,† the $CO_2$RR/$CO_2$ER overpotential of TiB/G reaches 2.43 V. During discharging, the potential-determining step (PDS) corresponds to the third electron transfer step (*i.e.*, the formation of carbon products), while the PDS during charging is the $Li_2CO_3$ decomposition on TiB/G surface. Notably, the introduction of Cu into the TiB/G plane effectively balances the adsorption and desorption of $Li_xC_yO_z$ ($x = 0$–2, $y = 1$–2, $z = 1$–3) reaction intermediates, leading to a shift in the PDS from the latter $2e^-$ transfer step to the initial $2e^-$ steps. Of greater interest is that the Cu/$Ti_{17}B_{18}$/G catalyst delivers a dramatically decreased $CO_2$RR/$CO_2$ER overpotential as low as 0.66 V (Fig. 3b). Fig. 3c summarizes the overpotentials of other excellent Li–$CO_2$ battery electrode catalysts. This performance

 This journal is © The Royal Society of Chemistry 2024

Published on 02 Waysu 2024. Downloaded on 28/07/2025 6:18:09 AM.

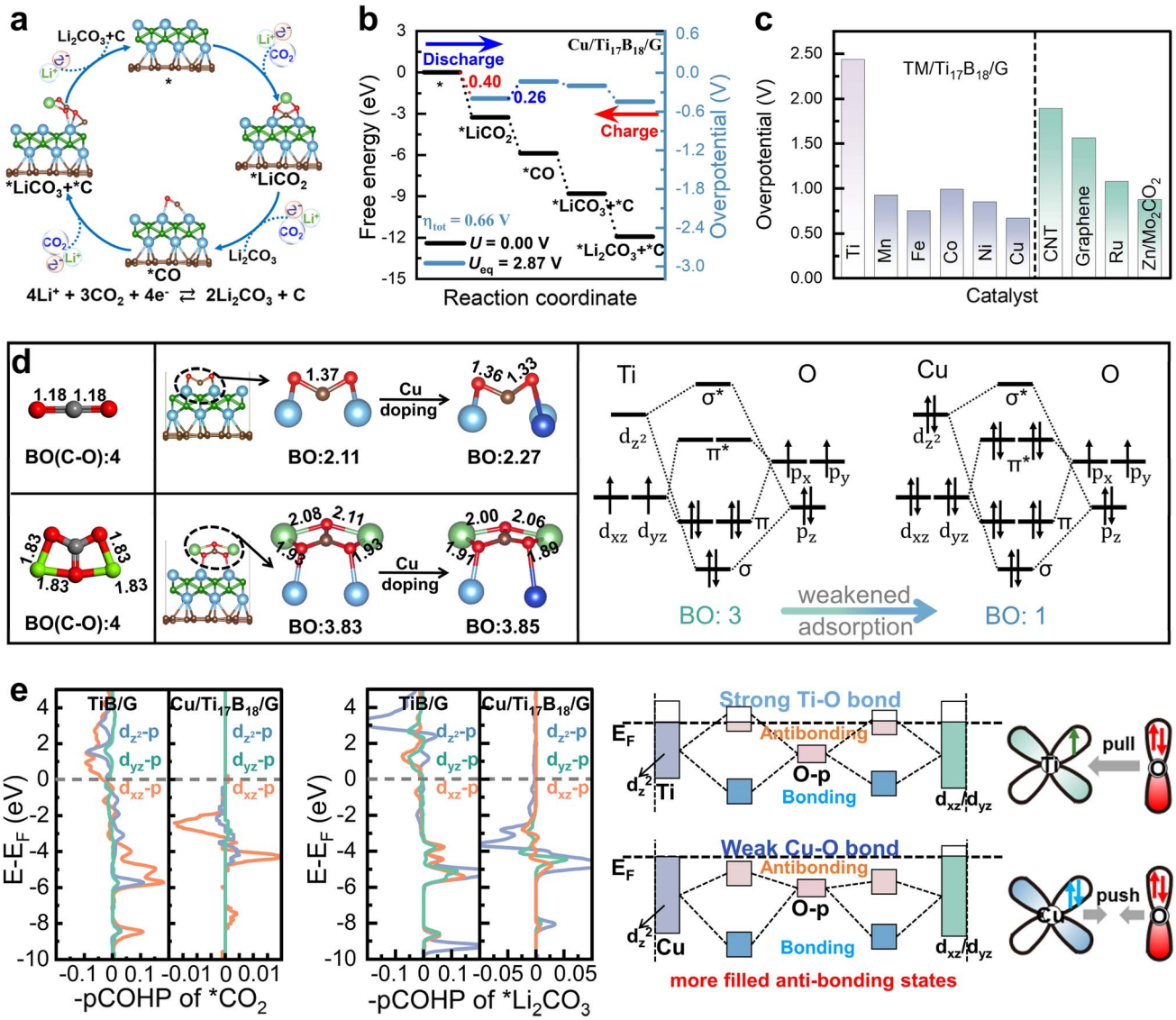


Fig. 3 (a) Continuous four-electron transfer pathway. (b) Free energy diagrams for Cu/$Ti_{17}B_{18}$/G, where blue and red numbers represent $CO_2$RR overpotential ($\eta_{CO_2RR}$) during discharge and $CO_2$ER overpotential ($\eta_{CO_2ER}$) during charge, respectively, and $\eta_{tot}$ represents the total overpotential. (c) Comparation of total overpotential with available references. (d) Cu as a dopant reducing bond order (BO) in $CO_2$ and $Li_2CO_3$ adsorbates. (e) Evolutions of bonding and antibonding states in p–d orbital interactions, where the spin-up and spin-down channels are identical in the projected crystal orbital Hamilton population (pCOHP) due to the zero magnetic moment of the system.

surpasses that of pristine TiB/G and previously reported carbon nanotubes (1.94 V), graphene (1.56 V),[57,58] noble metal Ru (1.07 V)[50] and single-atom modified MXenes like Zn/$Mo_2CO_2$ (0.97 V).[13] Besides, Fig. S6† depicts their Gibbs free energy for Li–$CO_2$ electrochemistry *via* a continuous $4e^-$ transfer pathway for other late transition metal modified TiB/G catalysts such as Mn, Fe, Co, and Ni. Remarkably, compared to pristine TiB/G ($\eta_{tot}$ = 2.43 V), the obtained Mn/$Ti_{17}B_{18}$/G, Fe/$Ti_{17}B_{18}$/G, Co/$Ti_{17}B_{18}$/G, and Ni/$Ti_{17}B_{18}$/G catalysts exhibit dramatically narrowed $CO_2$RR/$CO_2$ER overpotential as low as 0.92, 0.75, 0.99 and 0.84 V. This validates that doping engineering can be used as a guideline for the rational design of bifunctional electrocatalysts aimed at achieving reversible $CO_2$ and $Li_2CO_3$ conversion in Li–$CO_2$ batteries.

Given the pivotal role of $CO_2$ and $Li_2CO_3$ as reactants and products in Li–$CO_2$ batteries, we further explored the intricate relationship between p- and d-electron interactions and bifunctional activity at the atomic orbital level by focusing on their adsorption on TiB/G and Cu/$Ti_{17}B_{18}$/G surfaces. A striking similarity emerges: $CO_2$ and $Li_2CO_3$ are adsorbed *via* O p orbitals interacting with Ti or Cu d orbitals. As seen in Fig. S7,† there are three possible modes of p–d orbital interactions based on the principle of maximum overlap.[59] Specifically, the metal $d_{z^2}$ orbitals hybridize with the O $p_z$ orbitals to form σ bonds, whereas the $d_{xz}/d_{yz}$ orbitals hybridize with $p_x/p_y$ to form π bonds (Fig. 3d).[60] It is seen that the $d_{z^2}$, $d_{xz}$ and $d_{yz}$ electrons of Ti are occupied near the Fermi level (Fig. S8†), triggering the donation of d-electrons to the empty $CO_2$ antibonding orbitals,

Published on 02 Waysu 2024. Downloaded on 28/07/2025 6:18:09 AM.

yielding robust Ti–O bonding and excessive intermediate adsorption on the TiB/G plane. In sharp contrast, Cu d electrons are almost concentrated below the Fermi level (Fig. S9†) with a lower d-band center than Ti, yielding weakened interactions with O-containing intermediates. Further analysis of the projected crystal orbital Hamilton population (pCOHP) in Fig. 3e reveals that the orbital interactions between Cu d orbitals and O p orbitals induce more filled antibonding states below the Fermi level, indicating a weakened Cu–O bonding. Analogous trends are observed in the case of $Li_2CO_3$ adsorption. The reduced d-band center and increased antibonding state occupancy highlight the role of Cu dopants in mitigating the strong $Li_xC_yO_z$ adsorption on TiB/G. Therefore, the Cu/$Ti_{17}B_{18}$/G catalyst achieves enhanced bifunctional activity for the $CO_2$ reduction to $Li_2CO_3$ and its reversible conversion with carbon products.

### 3.3. Strain effects

We continue investigated the bifunctional catalytic performance of TiB/G and Cu/$Ti_{17}B_{18}$/G for $Li_2CO_3$ reversible conversion under uniaxial strain with a magnitude from −4% to +4%. The uniaxial stress–strain curves in Fig. S10a† illustrate that these TiB/G and Cu/$Ti_{17}B_{18}$/G materials can endure ultimate tensile strains of up to 22% and 26% along the *x*-direction, respectively, while withstanding up to 22% along the *y*-direction, delivering superior mechanical flexibility comparable to graphene. Furthermore, the differences in Young's modulus between the *x*- and *y*-directions (Fig. S10b†) highlight the anisotropic mechanical properties of TiB/G and Cu/$Ti_{17}B_{18}$/G.

Unlike transition metal doping, which significantly alters the PDS, applying uniaxial strain in the *x*-direction hardly changes the PDS for a given catalyst. As shown in Fig. S11 and S12,† the PDS during the discharge–charge process for TiB/G is almost maintained at the latter $2e^-$ transfer step under *x*-direction strain ranging from −4% to +4%, while the PDS for Cu/$Ti_{17}B_{18}$/G remains at the initial $2e^-$ transfer step. This indicates that the primary effect of *x*-direction strain is to lower the energy barrier of the PDS, rather than altering the PDS itself. This explains why the increase of d-band center under *x*-direction strain, which signifies stronger interactions with reaction intermediates,[61] results in a decrease in overpotential of the catalyst (Fig. 4a). Consequently, the overpotential for TiB/G decreases from 2.00 V to 1.83 V as strain varies from −4% to +4%, and for Cu/$Ti_{17}B_{18}$/G, it decreases from 0.72 V to 0.45 V. Similar enhancement of catalytic activity by strain engineering has been observed in other studies.[62,63]

In contrast, *y*-direction strain induces minimal changes in the d-band center, leading to a less significant impact on overpotential, as shown in Fig. 4b. The different strain effects in the *x*- and *y*-directions on overpotentials are due to the anisotropic mechanical properties of TiB/G and Cu/$Ti_{17}B_{18}$/G. As shown in Table S7† for TiB/G, the Young's modulus in the *y*-direction (562.5 N $m^{-1}$) is approximately 1.3 times higher than in the *x*-direction (431.6 N $m^{-1}$), which is much higher than that of isotropic materials like graphene (342 N $m^{-1}$) and $MoS_2$ (130 N $m^{-1}$).[64] This mechanical anisotropy, coupled with the ultrahigh Young's modulus, results in the relatively stable d-band center and overpotential for TiB/G and Cu/$Ti_{17}B_{18}$/G

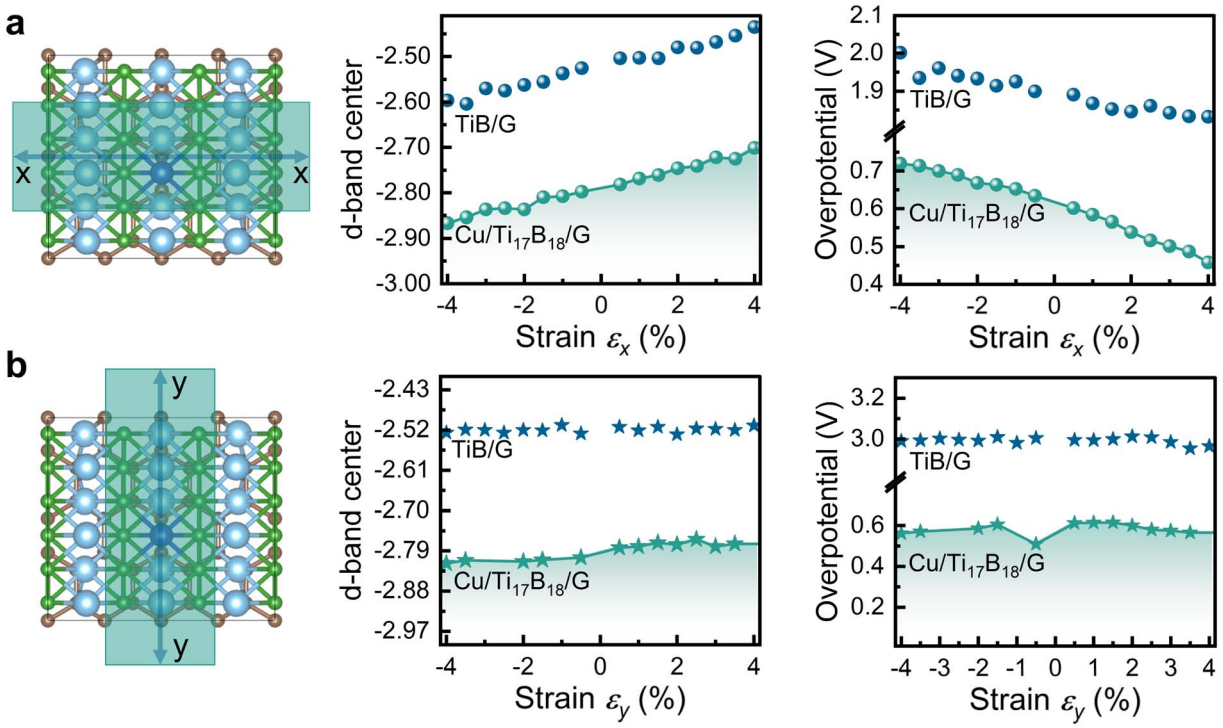


Fig. 4 The d-band centers ($\varepsilon_d$) shifts and overpotentials of TiB/G and Cu/$Ti_{17}B_{18}$/G under (a) *x*-direction and (b) *y*-direction strains with a magnitude from −4% to +4%.

 This journal is © The Royal Society of Chemistry 2024

Published on 02 Waysu 2024. Downloaded on 28/07/2025 6:18:09 AM.

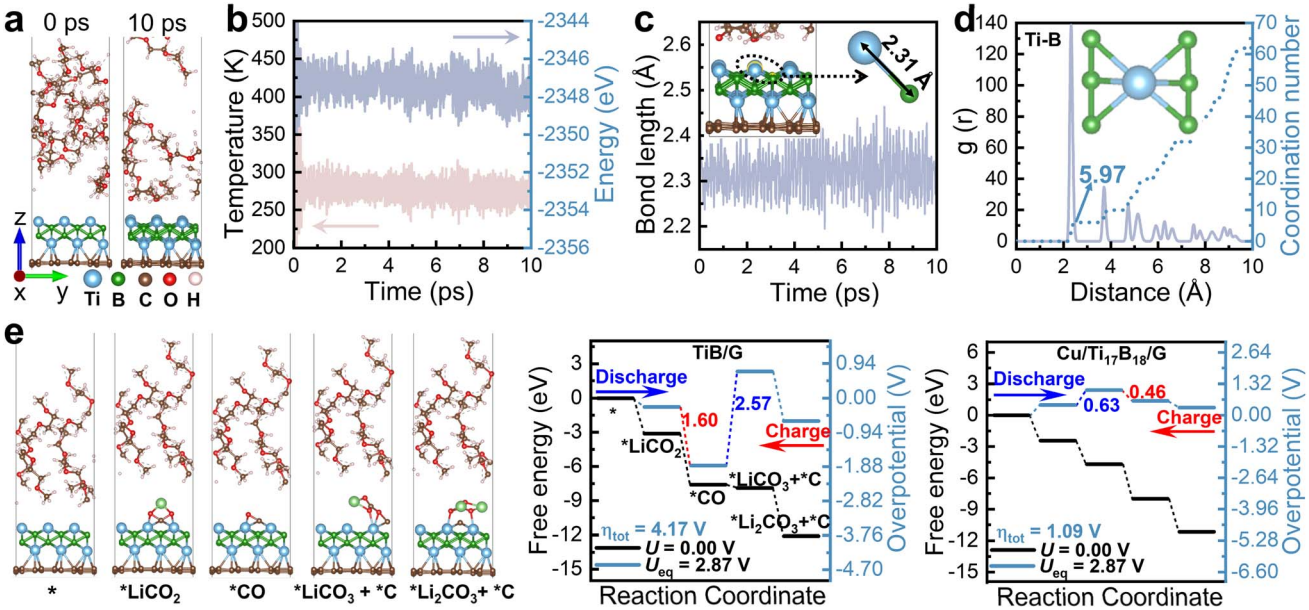


Fig. 5 (a–d) Evolutions of TiB/G structure, temperature and energy, Ti–B bond length, radial distribution function $g(r)$ and coordination number during AIMD simulations at 300 K. (e) Optimized intermediates and free energy diagrams under the explicit TEGDME solvent environment.

under external $y$-axial strains. Overall, direction-specific strain engineering, along with metal doping, proves to be an effective strategy for enhancing the bifunctional catalytic properties of TiB-based materials in Li–$CO_2$ batteries.

### 3.4. Stability in solution

To evaluate the durability of catalysts in an organic solvation medium, we assessed the thermal stability of TiB/G in a TEGDME solution at 300 K for 10 ps using AIMD simulations. TEGDME delivers flexible linear chain structure, low viscosity, and moderate dielectric constant (7.79) to enhance Li-ion mobility, making it an ideal solvent for Li–$CO_2$ batteries.[65,66] As shown in Fig. 5a, after 10 ps, the final TiB/G structure remained intact, with no bond breakage or structural rearrangement. Additionally, both temperature and total energy fluctuations were minimal, remaining within a narrow range (Fig. 5b). The Ti–B bond length maintained consistent at approximately 2.31 Å throughout the AIMD process (Fig. 5c). The radial distribution function $g(r)$, presented in Fig. 5d, indicates that the TiB/G heterostructure maintained excellent crystallization post-annealing, with Ti atoms predominantly coordinated by B atoms, and an average coordination number of approximately 5.97. These findings confirm that the TiB/G catalyst structure is robustly stable in the solution. Notably, the explicit solvent model depicted in Fig. 5e demonstrates that Cu doping significantly reduces the overpotential for $Li_2CO_3$ reversible conversion to 1.09 V, compared to 4.17 V for pristine TiB/G as Li–$CO_2$ battery catalyst.

The potential influence of other solvents, such as ethylene carbonate (EC) also examined. EC has a rigid cyclic structure, a high dielectric constant (approximately 90), and higher viscosity compared to TEGDME, which leads to strong interactions with lithium ions.[67] As shown in Fig. S13,† the AIMD results demonstrate that due to the presence of a carbon–oxygen ring with an ester linkage in EC molecules, EC strongly interacts with TiB/G over time, making EC unsuitable as a solvent for TiB-based catalysts in Li–$CO_2$ batteries. To provide a more solid reference to the experiments, the constant potential implicit solvent model[68,69] is employed to investigate the catalytic selectivity and bifunctional activity of both pristine and Cu-doped TiB/G catalysts (see ESI†).

## 4. Conclusions

In summary, we uncovered the origins of the enhanced activity of Cu-doped TiB MBene/graphene heterostructure in Li–$CO_2$ electrochemistry. By incorporating late transition metals with paired d electrons into the TiB/G structure, we achieved significantly improved bifunctional activity for the reversible conversion of $Li_2CO_3$. Specifically, the Cu/$Ti_{17}B_{18}$/G catalyst demonstrated an ultralow overpotential of 0.66 V for both $CO_2$ reduction and evolution reactions. This enhancement is attributed to the down-shifted d-band center and increased antibonding state occupancy in the $d_{z^2}$–$p_z$, $d_{xz}$–$p_x$ and $d_{yz}$–$p_y$ orbital hybridizations, which mitigates excessive intermediate adsorption on the TiB plane. Remarkably, applying tensile strain along the $x$-direction to the catalyst not only elevates its d-band center but also lowers the $CO_2$RR/$CO_2$ER overpotential, further boosting the bifunctional activity of Cu/$Ti_{17}B_{18}$/G for $Li_2CO_3$ conversion. Finally, AIMD simulations combined with explicit solvent models confirmed that these catalysts exhibit excellent electrochemical stability and durability in a practical solvent environment. This research highlights the critical role of tuning electronic structures through doping and strain engineering in the design of advanced catalysts, with potential applications across diverse fields.

Published on 02 Waysu 2024. Downloaded on 28/07/2025 6:18:09 AM.

## Data availability

The data supporting this article have been included as part of the ESI.† Raw data is available by contacting the corresponding author.

## Author contributions

Tingting Luo, Qiong Peng, Mengmeng Yang and Haojie Hu: conceptualization, investigation, visualization, methodology, writing – original draft. Junfei Ding, Yanli Chen and Xiu Gong: data curation, formal analysis, visualization. Jing-Liang Yang, Yunpeng Qu and Zeyou Zhou: supervision, writing – review & editing. Xiaosi Qi and Zhimei Sun: supervision, funding acquisition, resources, software. All authors contributed to the whole study.

## Conflicts of interest

The authors declare no conflict of interest.

## Acknowledgements

This work was financially supported by the National Natural Science Foundation of China (No. 52101010, 22005071 and 11964006), Natural Science Special (Special Post) Research Foundation of Guizhou University (No. 2020-020), Platform of Science and Technology and Talent Team Plan of Guizhou province (No. GCC[2023]007), Fok Ying Tung Education Foundation, Major Research Project of innovative Group of Guizhou province (No. 2018-013), Natural Science Foundation of Guizhou province [No. ZK 2022-044].

## References

1 Y. Liu, P. Shu, M. Zhang, B. Chen, Y. Song, B. Lu, R. Mao, Q. Peng, G. Zhou and H.-M. Cheng, *ACS Energy Lett.*, 2024, **9**, 2173–2181.
2 D. Wang, J. Yang, P. He and H. Zhou, *Energy Environ. Sci.*, 2021, **14**, 4107–4114.
3 J. Lin, J. Ding, H. Wang, X. Yang, X. Zheng, Z. Huang, W. Song, J. Ding, X. Han and W. Hu, *Adv. Mater.*, 2022, **34**, 2200559.
4 J. Chen, X.-Y. Chen, Y. Liu, Y. Qiao, S.-Y. Guan, L. Li and S.-L. Chou, *Energy Environ. Sci.*, 2023, **16**, 792–829.
5 Y. Yang, K. Guo, D. Yuan, J. Cheng and B. Wang, *J. Am. Chem. Soc.*, 2020, **142**, 6983–6990.
6 Y. Wang, J. Zhou, C. Lin, B. Chen, Z. Guan, A. M. Ebrahim, G. Qian, C. Ye, L. Chen, Y. Ge, Q. Yun, X. Wang, X. Zhou, G. Wang, K. Li, P. Lu, Y. Ma, Y. Xiong, T. Wang, L. Zheng, S. Chu, Y. Chen, B. Wang, C.-S. Lee, Y. Liu, Q. Zhang and Z. Fan, *Adv. Funct. Mater.*, 2022, **32**, 2202737.
7 X. Zhang, Y. Wang and Y. Li, *J. Phys. Chem. Lett.*, 2023, **14**, 1604–1608.
8 X. Xiao, Z. J. Zhang and P. Tan, *Proc. Natl. Acad. Sci. U. S. A.*, 2023, **120**, e2217454120.
9 S. Chen, K. Yang, H. Zhu, J. Wang, Y. Gong, H. Li, M. Wang, W. Zhao, Y. Ji, F. Pan, S. R. P. Silva, Y. Zhao and L. Yang, *Nano Energy*, 2023, **117**, 108872.
10 J. Zhou, T. Wang, L. Chen, L. Liao, Y. Wang, S. Xi, B. Chen, T. Lin, Q. Zhang, C. Ye, X. Zhou, Z. Guan, L. Zhai, Z. He, G. Wang, J. Wang, J. Yu, Y. Ma, P. Lu, Y. Xiong, S. Lu, Y. Chen, B. Wang, C. S. Lee, J. Cheng, L. Gu, T. Zhao and Z. Fan, *Proc. Natl. Acad. Sci. U. S. A.*, 2022, **119**, e2204666119.
11 R. Huang, Z. Zhai, X. Chen, Q. Liu, H. Yu, B. Li and S. Yin, *Chem. Eng. J.*, 2024, **489**, 151191.
12 J. Xie, Z. Zhou and Y. Wang, *Adv. Funct. Mater.*, 2020, **30**, 1908285.
13 Y. Shi, B. Wei, D. Legut, S. Du, J. S. Francisco and R. Zhang, *Adv. Funct. Mater.*, 2022, **32**, 2210218.
14 B. Lu, X. Wu, X. Xiao, B. Chen, W. Zeng, Y. Liu, Z. Lao, X.-X. Zeng, G. Zhou and J. Yang, *Adv. Mater.*, 2024, **36**, 2308889.
15 J. Zhou, X. Li, C. Yang, Y. Li, K. Guo, J. Cheng, D. Yuan, C. Song, J. Lu and B. Wang, *Adv. Mater.*, 2019, **31**, 1804439.
16 T. Xu, Y. Wang, Z. Xiong, Y. Wang, Y. Zhou and X. Li, *Nano-Micro Lett.*, 2023, **15**, 6.
17 X. Bai, Z. Zhao and G. Lu, *J. Phys. Chem. Lett.*, 2023, **14**, 5172–5180.
18 T. Zhang, B. Zhang, Q. Peng, J. Zhou and Z. Sun, *J. Mater. Chem. A*, 2021, **9**, 433–441.
19 M. Zafari, A. S. Nissimagoudar, M. Umer, G. Lee and K. S. Kim, *J. Mater. Chem. A*, 2021, **9**, 9203–9213.
20 S. H. Mir, V. K. Yadav and J. K. Singh, *ACS Appl. Mater. Interfaces*, 2022, **14**, 29703–29710.
21 M. Ozkan, K. A. M. Quiros, J. M. Watkins, T. M. Nelson, N. D. Singh, M. Chowdhury, T. Namboodiri, K. R. Talluri and E. Yuan, *Chem*, 2024, **10**, 443–483.
22 P. Shu, Q. Peng, T. Luo, J. Ding, X. Gong, J. Zhou, Y. Yu, X. Qi and Z. Sun, *J. Mater. Chem. A*, 2024, **12**, 6515–6526.
23 W. Guo, X. Tan, S. Jia, S. Liu, X. Song, X. Ma, L. Wu, L. Zheng, X. Sun and B. Han, *CCS Chem.*, 2024, **6**, 1231–1239.
24 Y. Yang, S. Louisia, S. Yu, J. Jin, I. Roh, C. Chen, M. V. Fonseca Guzman, J. Feijóo, P.-C. Chen, H. Wang, C. J. Pollock, X. Huang, Y.-T. Shao, C. Wang, D. A. Muller, H. D. Abruña and P. Yang, *Nature*, 2023, **614**, 262–269.
25 G. Kresse and J. Furthmüller, *Phys. Rev. B*, 1996, **54**, 11169.
26 J. Hafner, *J. Comput. Chem.*, 2008, **29**, 2044–2078.
27 G. Kresse, *J. Non-Cryst. Solids*, 1995, **192–193**, 222–229.
28 G. Wang, L.-q. Peng, K. Li, L. Zhu, J. Zhou, N. Miao and Z. Sun, *Comput. Mater. Sci.*, 2021, **186**, 110064.
29 V. Wang, N. Xu, J.-C. Liu, G. Tang and W.-T. Geng, *Comput. Phys. Commun.*, 2021, **267**, 108033.
30 S. Grimme, J. Antony, S. Ehrlich and H. Krieg, *J. Chem. Phys.*, 2010, **132**, 154104.
31 L. Liu and H. Xiao, *J. Am. Chem. Soc.*, 2023, **145**, 14267–14275.
32 S. Steinberg and R. Dronskowski, *Crystals*, 2018, **8**, 225.
33 R. F. W. Bader, *Chem. Rev.*, 1991, **91**, 893–928.
34 G. Henkelman, A. Arnaldsson and H. Jónsson, *Comput. Mater. Sci.*, 2006, **36**, 354–360.
35 G. Henkelman, B. P. Uberuaga and H. Jónsson, *J. Chem. Phys.*, 2000, **113**, 9901–9904.

 This journal is © The Royal Society of Chemistry 2024

Published on 02 Waysu 2024. Downloaded on 28/07/2025 6:18:09 AM.

36 S. Nosé, *J. Chem. Phys.*, 1984, **81**, 511–519.
37 C. Laoire, S. Mukerjee, E. J. Plichta, M. A. Hendrickson and K. M. Abraham, *J. Electrochem. Soc.*, 2011, **158**, A302.
38 M. A. Rivas, T. P. Iglesias, S. M. Pereira and N. Banerji, *J. Chem. Thermodyn.*, 2006, **38**, 245–256.
39 J. Holoubek, H. Liu, Z. Wu, Y. Yin, X. Xing, G. Cai, S. Yu, H. Zhou, T. A. Pascal, Z. Chen and P. Liu, *Nat. Energy*, 2021, **6**, 303–313.
40 G. N. Greaves, A. L. Greer, R. S. Lakes and T. Rouxel, *Nat. Mater.*, 2011, **10**, 823–837.
41 Y. Zhu and X. Wu, *Prog. Mater. Sci.*, 2023, **131**, 101019.
42 B. Mortazavi, M. Silani, E. V. Podryabinkin, T. Rabczuk, X. Zhuang and A. V. Shapeev, *Adv. Mater.*, 2021, **33**, 2102807.
43 Q. Peng, K. Hu, B. Sa, J. Zhou, B. Wu, X. Hou and Z. Sun, *Nano Res.*, 2017, **10**, 3136–3150.
44 Y. Luo, Z. Ma, X. Xia, J. Zhong, P. Wu and Y. Huang, *ChemSusChem*, 2023, **16**, e202202209.
45 J. Cho, A. Medina, I. Saih, J. Il Choi, M. Drexler, W. A. Goddard Iii, F. M. Alamgir and S. S. Jang, *Angew. Chem., Int. Ed.*, 2024, **63**, e202320268.
46 P. Shu, X. Qi, Q. Peng, Y. Chen, X. Gong, Y. Zhang, F. Ouyang and Z. Sun, *Mol. Catal.*, 2023, **539**, 113036.
47 S. Jiao, X. Fu and H. Huang, *Adv. Funct. Mater.*, 2022, **32**, 2107651.
48 J. K. Nørskov, F. Abild-Pedersen, F. Studt and T. Bligaard, *Proc. Natl. Acad. Sci. U. S. A.*, 2011, **108**, 937–943.
49 Y. Hou, J. Wang, L. Liu, Y. Liu, S. Chou, D. Shi, H. Liu, Y. Wu, W. Zhang and J. Chen, *Adv. Funct. Mater.*, 2017, **27**, 1700564.
50 J. Hu, C. Yang and K. Guo, *J. Mater. Chem. A*, 2022, **10**, 14028–14040.
51 W. Zhao, Y. Yang, Q. Deng, Q. Dai, Z. Fang, X. Fu, W. Yan, L. Wu and Y. Zhou, *Adv. Funct. Mater.*, 2023, **33**, 2210037.
52 X. Sun, X. Mu, W. Zheng, L. Wang, S. Yang, C. Sheng, H. Pan, W. Li, C. H. Li, P. He and H. Zhou, *Nat. Commun.*, 2023, **14**, 536.
53 A. Ahmadiparidari, R. E. Warburton, L. Majidi, M. Asadi, A. Chamaani, J. R. Jokisaari, S. Rastegar, Z. Hemmat, B. Sayahpour, R. S. Assary, B. Narayanan, P. Abbasi, P. C. Redfern, A. Ngo, M. Vörös, J. Greeley, R. Klie, L. A. Curtiss and A. Salehi-Khojin, *Adv. Mater.*, 2019, **31**, 1902518.
54 Y. Liu, R. Mao, B. Chen, B. Lu, Z. Piao, Y. Song, G. Zhou and H. M. Cheng, *Mater. Today*, 2023, **63**, 120–136.
55 Y. Liu, S. Zhao, D. Wang, B. Chen, Z. Zhang, J. Sheng, X. Zhong, X. Zou, S. P. Jiang, G. Zhou and H. M. Cheng, *ACS Nano*, 2022, **16**, 1523–1532.
56 B. Chen, D. Wang, J. Tan, Y. Liu, M. Jiao, B. Liu, N. Zhao, X. Zou, G. Zhou and H.-M. Cheng, *J. Am. Chem. Soc.*, 2022, **144**, 3106–3116.
57 S. Li, Y. Dong, J. Zhou, Y. Liu, J. Wang, X. Gao, Y. Han, P. Qi and B. Wang, *Energy Environ. Sci.*, 2018, **11**, 1318–1325.
58 Z. Zhang, Q. Zhang, Y. Chen, J. Bao, X. Zhou, Z. Xie, J. Wei and Z. Zhou, *Angew. Chem., Int. Ed.*, 2015, **54**, 6550–6553.
59 Y. Qian, Y. Liu, Y. Zhao, X. Zhang and G. Yu, *EcoMat*, 2020, **2**, e12014.
60 Q. Jing, Z. Mei, X. Sheng, X. Zou, Q. Xu, L. Wang and H. Guo, *Adv. Funct. Mater.*, 2024, **34**, 2307002.
61 M. Gsell, P. Jakob and D. Menzel, *Science*, 1998, **280**, 717–720.
62 Y. Yan, J. Lin, K. Huang, X. Zheng, L. Qiao, S. Liu, J. Cao, S. C. Jun, Y. Yamauchi and J. Qi, *J. Am. Chem. Soc.*, 2023, **145**, 24218–24229.
63 C. Zhao, Y. Huang, B. Jiang, Z. Chen, X. Yu, X. Sun, H. Zhou, Y. Zhang and N. Zhang, *Adv. Energy Mater.*, 2024, **14**, 2302586.
64 Q. Peng, Z. Guo, B. Sa, J. Zhou and Z. Sun, *Int. J. Hydrogen Energy*, 2018, **43**, 15995–16004.
65 X.-P. Zhang, Y.-N. Li, Y.-Y. Sun and T. Zhang, *Angew. Chem., Int. Ed.*, 2019, **58**, 18394–18398.
66 Y. Chen, J. Li, B. Lu, Y. Liu, R. Mao, Y. Song, H. Li, X. Yu, Y. Gao, Q. Peng, X. Qi and G. Zhou, *Adv. Mater.*, 2024, DOI: **10.1002/adma.202406856**.
67 N. Lespes and J.-S. Filhol, *J. Chem. Theory Comput.*, 2015, **11**, 3375–3382.
68 L. Miao, W. Jia, X. Cao and L. Jiao, *Chem. Soc. Rev.*, 2024, **53**, 2771–2807.
69 X. Hu, S. Chen, L. Chen, Y. Tian, S. Yao, Z. Lu, X. Zhang and Z. Zhou, *J. Am. Chem. Soc.*, 2022, **144**, 18144–18152.